

Surface-radical Mobility Test by Self-sorted Recombination: Symmetrical Product upon Recombination (SPR)

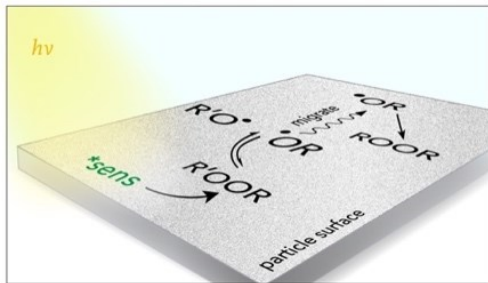
Sarah J. Belh,^{1,2} Goutam Ghosh,^{1,2} and Alexander Greer^{1,2*}

¹ Department of Chemistry, Brooklyn College, 2900 Bedford Avenue, Brooklyn, New York 11210, United States

² Ph.D. Program in Chemistry, The Graduate Center of the City University of New York, 365 Fifth Avenue, New York, New York 10016, United States

E-mail: agreeer@brooklyn.cuny.edu

TOC Graphic



Abstract

We describe here a study of the mobility of alkoxy radical on a surface by detection of its recombination product. A novel method called symmetrical product recombination (SPR) uses an unsymmetrical peroxide that upon sensitized homolysis recombines to a symmetrical product $[R'OR \rightarrow R'O\cdot \uparrow + \cdot OR \rightarrow ROOR]$. This allows for self-sorting of the radical to enhance the

recombination path to a symmetrical product, which has been used to deduce surface migratory aptitude. SPR also provides a new opportunity for mechanistic studies of interfacial radicals, including monitoring competition between radical recombination versus surface hydrogen abstraction. This is an approach that might work for other surface-born radicals on natural and artificial particles.

Introduction

Nanoparticle surfaces can have advantages over homogeneous solution for the control of radical reactions. For example, surfaces may be tuned to selective reactions by controlling radical mobility. However, mechanistic studies on surface-bound radicals, such as alkoxy radicals, are still challenging. While such information is typically sought with EPR trapping¹⁻⁴ and ³¹P NMR spectroscopy,⁵ the goal to expand on methods to measure radical migratory aptitude is a needed area of research. Here, we report a symmetrical product recombination (SPR) method that allows the determination of alkoxy radical surface mobility by a symmetrical product from an unsymmetrical substrate [R'OOR → R'O• + •OR → ROOR] (Figure 1). This approach is demonstrated here for alkoxy radicals, but might also work for other radicals.

Radicals can form on artificial⁶⁻⁸ and natural surfaces.⁹⁻¹¹ Some environmental reactions take place with particulate formation of persistent radicals.¹²⁻¹⁵ Thus, developing a trapping system that can assess surface migration is desirable.

Researchers have developed various methods for monitoring of radical reactions on surfaces. One method is EPR spectroscopy¹⁶ by analyzing the hyperfine tensor for the interaction between the radical and surrounding magnetic nuclei. A second approach is theoretical, for

example a $\text{H}_3\text{Si}\cdot$ diffusion activation barrier on silicon was found to be 3.7 kcal/mol by DFT and MD simulations.¹⁷ A third approach is the use of ^{31}P NMR spectroscopy with phosphite traps^{5,18} due to their oxophilicity to trap alkoxy radicals. In the third approach, alkoxy radicals on silica nanoparticles were trapped by phosphites to form phosphates. In the present article, the SPR method can help to advance the field to deduce the migratory aptitude of radicals on a particle surface.

We now report on a new concept for generating a scrambled product that probes the lateral diffusion of alkoxy radicals on a silica nanoparticle. A photoexcited 4,4'-dimethylbenzil sensitizer **1** is used to homolyze an unsymmetrical peroxide **2** (Figure 2). The resulting homolysis leads to alkoxy radicals that can recombine to a symmetrical peroxide **3**. We find that the symmetrical product **3** formation depends on the loading quantity of substrate **2** that is used. We find that radical migration distance reaches a maximum of 2.9 nm on the nanoparticle surface, suggesting the usefulness of this approach for surface diffusion studies of alkoxy radicals. A self-sorting preference is also predicted by DFT calculations and mathematical deductions.

The SPR approach fulfills two functions in this nanoparticle reaction. First, it ensures migration of a molecular radical. This enables assessment of the radical ability to *translocate* on the surface, rather than *propagate* as in $\text{L}\cdot$ (location 1) + LH (location 2) \rightarrow LH (location 1) + $\text{L}\cdot$ (location 2), as is needed to assess migration patterns of molecular radicals. Second, the chain termination of radicals provides a way to promote signal intensity within a symmetrical compound by ^1H NMR spectroscopy, as used to advantage in structure determination of natural products bearing molecular bilateral symmetry.^{19,20} Furthermore, the SPR approach is a novel

peroxide scrambling strategy that provides insight to both the translation *and* volatility of radicals.

A mechanism is proposed in Figure 2, in which photosensitization triggers the unsymmetrical peroxide **2** to homolyze, with the higher molecular weight $\text{PhC}(\text{Me})_2\text{O}^\bullet$ radical of the pair remains adsorbed, and thus generating a symmetrical peroxide **3** to monitor. This supports a mechanistic hypothesis that radical recombination is detected from $\text{PhC}(\text{Me})_2\text{O}^\bullet$ radical pairing on the nanoparticle surface. Further, it shows that the product signal is symmetry increased for ^1H NMR spectroscopy, and not obscured by chain propagation products, as is often seen in homogeneous solution. The SPR method that we developed can potentially be used in combination with EPR methods for better insight into mobility and reactions of radicals on surfaces.

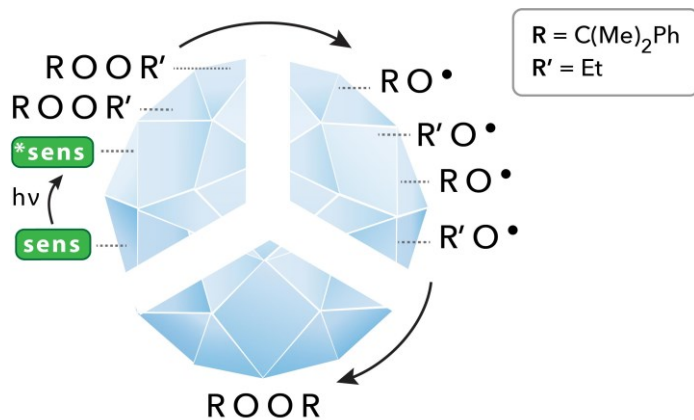


Figure 1. Schematic of alkoxy radical migration on a nanoparticle [$\text{R} = \text{C}(\text{Me}_2)\text{Ph}$; $\text{R}' = \text{Et}$]. The radical production is via cumylethyl peroxide's photosensitized O–O homolysis, including alkoxy radical migration, and formation of a symmetrical ROOR product. Symmetrical ROOR

product formation is favored, whereas chain propagation processes, for example H-atom transfer are disfavored.

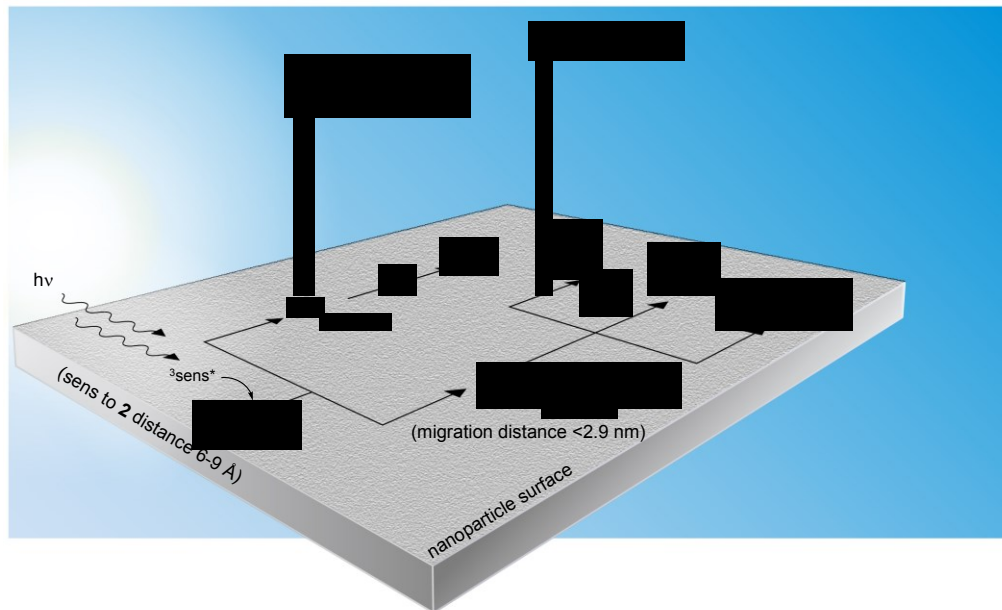


Figure 2. Proposed paths for the photosensitized homolysis of cumylethyl peroxide **2** at the gas/nanoparticle interface. Concentrations of alkoxy radicals forming a symmetrical peroxide product **3** increase at the air/solid interface as $\text{EtO}\cdot$ and $\text{CH}_3\cdot$ fragments volatilize away from the surface. A two-phase sensitized photolysis of a lighter peroxide, which induces this combination of heavier alkoxy radicals to provide mechanistic details to radical mobility on a surface. An additional scheme with structure drawings is shown in Figure S4 (Supporting Information).

Results and Discussion

Products of the Reaction. Nanoparticles co-adsorbed with 4,4'-dimethylbenzil (sensitizer **1**) and cumylethyl peroxide **2** were irradiated with ($280 < \lambda < 700$ nm) light in a N_2 -degassed glass vessel. Five products were detected in the photoreaction (Table 1). The products were dicumyl peroxide **3**, cumyl alcohol **4**, and acetophenone **5**, as detected by HPLC upon desorbing products from the nanoparticle surface. Ethanal **6** and methane **7** can be detected by ^1H NMR spectroscopy when analyzing the headspace or in a solution-phase photoreaction containing dissolved sensitizer **1** and cumylethyl peroxide **2**. Diethyl peroxide **8** was not detected with our HPLC and ^1H NMR spectroscopic analyses. Reversible dimerization from primary products **3** and **8** does not yield **2** in high yields, apparently because the $\text{EtO}\cdot$ is sufficiently volatile to disconnect from the surface. The reaction allows for a radical mobility test because it forms the bilaterally symmetrical dicumyl peroxide **3** from recombination of cumyloxy radicals. This is somewhat reminiscent to bilaterally symmetric 1,2-di-*p*-tolylethane and 1,2-bis(4-methoxyphenyl)ethane from the radical combination of *p*-xylene radical and 1-methoxy-4-methylbenzene radical, respectively, in the photolysis of silica-adsorbed 1-(4-methylphenyl)-3-(4-methoxyphenyl)-2-propanone.²¹

Table 1. Product distribution (%) for the sensitized homolysis of cumylethyl peroxide **2** that generates oxygen- and carbon-centered radicals and stable products.^a

	relative yields ^{b,c}	
	conditions A	condition B ^d

entry	peroxide 2 adsorbed ($\mu\text{mol/g}$)	dicumyl peroxide 3	cumyl alcohol 4	acetophenone 5	ethanal 6	methane 7
1	108 ^e	25.2 \pm 0.5	12.7 \pm 0.1	12.4 \pm 0.02	12.4	37.3
2	53.2	18.2 \pm 1.0	14.9 \pm 0.1	13.8 \pm 0.1	13.3	39.8
3	27.1	11.8 \pm 0.8	15.9 \pm 0.2	15.3 \pm 0.2	14.6	43.7
4	13.4	9.8 \pm 0.6	14.9 \pm 0.4	17.6 \pm 1.3	14.4	43.2
5	6.78	4.0 \pm 2.4	13.2 \pm 1.6	16.7 \pm 0.7	16.5	49.6

^a Selective irradiation of 4,4'-dimethylbenzil sensitizer **1** (330 $\mu\text{mol/g}$ silica) with (280 $< \lambda <$ 700 nm) light was carried out in the presence of cumylethyl peroxide **2** co-adsorbed on particles. ^b Relative yields determined by HPLC or ¹H NMR spectroscopy and were based on their integrated peak areas without the use of an external standard. Relative yields of product at the air/solid interface relative to solution-phase conditions. ^c Condition A: air/solid interface; condition B: homogeneous photoreaction of sensitizer **1** (0.01 mM) and peroxide **2** (0.1 mM) in acetonitrile-*d*₃ irradiated in an NMR tube. ^d The experimental error in condition B is \pm 5%. ^e A control photoreaction of cumylethyl peroxide **2** (108 $\mu\text{mol/g}$) with (280 $< \lambda <$ 700 nm) light in the absence of sensitizer **1** led to \sim 0.002% peroxide **3**.

Radical Mobility Test. Here, sensitizer **1** was used to homolyze **2**, where we use radical recombination to symmetrical product **3** was used as a test for radical mobility on the nanoparticle surface. Eq 1 shows the calculated number of **1** or **2** molecules adsorbed on the particle surface using Avogadro's number (N_A). Eq 2 shows the average distance between adsorbed **1** or **2** molecules with the assumption that there is a pristine nanoparticle surface. Further, occupation of sites by sensitizer molecules are calculated to be negligible, where the **2**-to-**2** distances decrease by 0.027 nm for 108 μmol **2**/g nanoparticle and by <0.001 nm for 6.78 μmol **2**/g nanoparticle. Eq 3 is used in conjunction with eq 2 to deduce the radical migration distance upon recombination to symmetrical **3**. The shape of the cumyloxy radical is a rectangle (0.71 nm \times 0.43 nm), in which the average of its width and length were used in eq 3 (0.58 nm). The **2**-to-**2** distance is based on the amount of **2** adsorbed on the nanoparticles, and not based on a recalculated yield of **3**. Eq 4 shows the calculation for the percent particle coverage of **1** or **2**. Cumyloxy radicals were generated and recombined to **3** in amounts ranging from a high of 25.2% to a low of 4.0% yield (Table 1, entries 1 and 5). This led to the calculated surface migration distance of cumyloxy radical on the nanoparticle of 0.27 nm up to a maximum of 2.9 nm (Figure 3). The selectivity is not caused by heating of the reaction. The nanoparticle photoreactions were carried out at 26 °C. During the photolysis, the particles increased in temperature by ~10 °C. This temperature rise is insufficient to cause the thermolysis of **2** or **3**, based on control reactions, where thermolysis temperatures of 130 °C would have been required.²² A weaker peroxide, benzoyl peroxide, requires heating above 80 °C to split into benzoyl radicals, which in turn form phenyl radicals and CO₂.²³ Next, we compute the difference in O–O bond strength of **2** relative to **3** to help rationalize selectivity for the high yields of the product **3**.

$$\text{molecule to molecule distance (nm)} = \sqrt{\frac{\text{particle surface area (nm}^2/\text{g)}}{\text{molecules of 1 or 2}}} \quad \dots \dots \dots \quad (2)$$

$$\text{radical migration distance (nm)} = \frac{2\text{-to-2 distance (nm)}}{2} - 2 \text{ length (nm)} \dots \dots \dots (3)$$

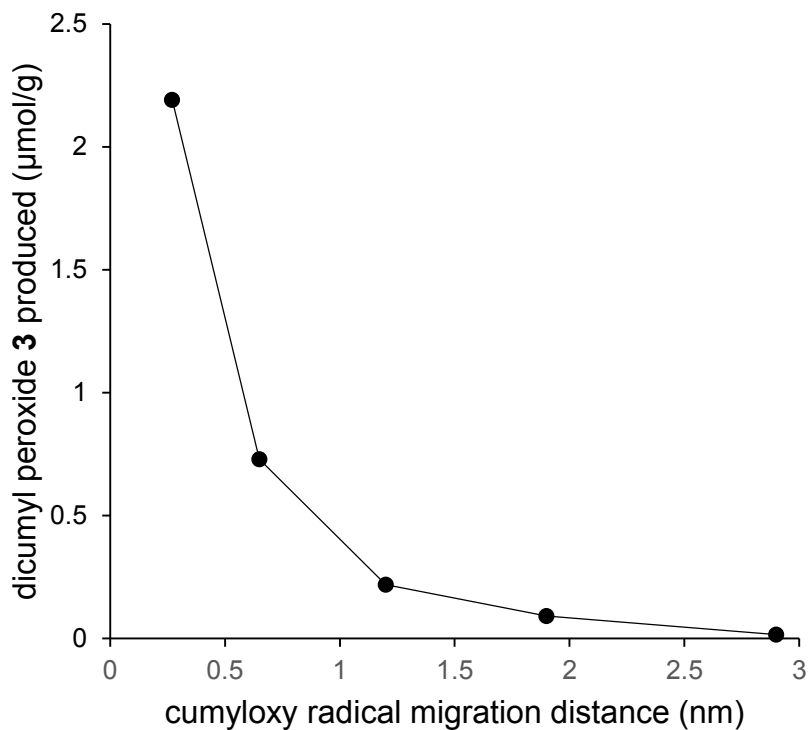


Figure 3. Correlation of dicumyl peroxide **3** with cumyloxy radical migration distance on the nanoparticles that arose by the sensitized homolysis of **2**.

Radical “Self-Sorting”. Unrestricted M06-2X/6-31G(d,p) calculations are used to help explain the selective formation of the O–O bond in dicumyl peroxide **3**. The DFT method employed here is found to reproduce experimental O–O bond dissociation energies of organic peroxides.²⁴ Our DFT study was designed to assess the geometries and bonding based on the influence the PhC(Me)₂ and Et groups impart on peroxides **2**, **3**, and **8**, and radicals PhC(Me)₂O• and EtO•, and also rationalize possible interfacial effects. While calculations of surface energies were not carried out, our experimental results of preferred H-transfer to PhC(Me)₂O• and H-atom loss from EtO• provide a degree of justification for our use of DFT gas phase calculations in modeling the surface process, as we will see.

Peroxides **2**, **3**, and **8**, and their corresponding alkoxy radicals PhC(Me)₂O• and EtO• optimized to minima. The calculated torsion angle θ (C–O–O–C) of **3** is increased (178.0°) when compared to **2** (124.8°) and **8** (109.9°). As the size of the substituent of the peroxide increases (**8** < **2** < **3**), then rotation about this torsion θ energy is increased, as we will see. To explore the energy associated with rotation around the θ torsion angle, minima and transition structures (TS) were located on the potential energy surface. Rotation around the θ torsion angle among *gauche* and *anti* geometries changed the energy by 3.5 kcal/mol (for **3**), whereas it only changed by 0.63 kcal/mol (for **2**), and 0.43 kcal/mol (for **8**). The larger PhC(Me)₂ substituent at the O–O bond increases the activation barrier that yields full rotation. Rotating the θ torsion angle where they adopt a *syn* TS geometry was large 28.0 kcal/mol for **3** (due to destabilizing PhC(Me)₂/PhC(Me)₂

interactions, whereas the TS is 19.3 kcal/mol for **2** (due to modestly destabilizing PhC(Me)₂/Et interactions), and even less at 11.2 kcal/mol for the TS of **8** (due to less destabilizing Et/Et interactions). The substituent effects that influence the structures can also influence the bond energies.

Thus, next we investigated the energetics for O–O bond homolysis. The O–O bond in peroxides is weak due in part to electronic repulsion of lone pairs on the adjacent oxygen atoms. The π MO is strong between the two oxygen atoms, and the antibonding π^* is destabilizing. Endothermicity increases for **3** (due to a stronger O–O) than in **2** and **8**. The endothermicity of **3** relative to 2 PhC(Me)₂O \bullet (39.2 kcal/mol) is greater than PhC(Me)₂OOEt **2** relative to PhC(Me)₂O \bullet and EtO \bullet (37.4 kcal/mol), and EtOOEt **8** relative to 2 EtO \bullet (37.6 kcal/mol). The presence of electron delocalization of **3** may explain its greater stability than peroxides **2** and **8** with one or two ethyl groups. It has been noted in the literature that substituting the R group Et for Ph (slight electron withdrawing group)²⁵ in Me₃CO–OC(Me)₂R leads to a 0.1 kcal/mol stabilization of the peroxide bond.²⁶ Similarly, substituting the R group Et for CF₃ (the latter is a strong EWG) in RO–OR leads to a 15.9 kcal/mol stabilization of the peroxide bond.^{26,27} Also, substituting the *p*-X-substituent (X = MeO for X = NO₂) in *p*-X-C₆H₄-C(Me)₂O–OCMe₃ leads to a 0.4 kcal/mol stabilization of the peroxide bond.²⁶ Further details underlying the stabilities of peroxides have been recently rationalized in detail.²⁸

The above computed data suggests self-sorting capacity in higher thermal O–O bond energy in **3** than **2** or **8**, is complementary to volatility in terms of binding affinity and selective binding. Namely, dicumyl peroxide **3** is adsorbed more tightly to the particle surface than **2** and **8** due to its two phenyl rings. Our computed show the formation of a OH \cdots π bond between (HO)₃SiOH and benzene in the gas phase is 6.0 kcal/mol, and has a perpendicular orientation to

the plane of the aromatic ring, at the point of plane interaction by a lengthened O–H bond. The DFT prediction is that the phenyls of $\text{PhC}(\text{Me})_2\text{O}\cdot$, **2** and **3**, are bonded in a π -hydrogen bond to the surface SiOH groups, has been confirmed experimentally for naphthacene.²⁹ This is known to be stabilizing with a decreased HOMO-LUMO energy gap and an increased dipole moment. These π -hydrogen bonds are often comparable in strength to conventional H-bonding.³⁰⁻³² Our DFT results indicate that the $\text{EtO}\cdot$ is weakly bonded to the SiOH group. We suggest that the $\text{SiOH}\cdots\pi(\text{aromatic ring})$ hydrogen bonding will increase the adsorption energy, that along with the increased molecular weight underlie the lower volatilization of $\text{PhC}(\text{Me})_2\text{O}\cdot$ compared to $\text{EtO}\cdot$, thereby facilitating self-sorting to reach **3**. The $\text{RO}\cdot\cdots\text{OR}$ binding process was shown to be barrierless, while the desorptive volatility process has a barrier of ~ 2 kcal/mol for low molecular weight compounds. But what about to the competition with H abstraction?

Radical H-atom Abstraction. The radicals can abstract from the SiOH groups or adsorbed water on the nanoparticle surface. Here, we draw on a relationship between electronegativity of radicals and whether they abstract H or dimerize, a concept borrowed in a different vein to the context of H-abstraction versus alkene addition.³³⁻³⁶ Table 2 shows that the electronegativity can be used to assess the paths of radicals as measured by calculation of $(\text{IP} + \text{EA})/2$. $\text{PhC}(\text{Me})_2\text{O}\cdot$ and $(\text{MeO})_3\text{SiO}\cdot$ are relatively electropositive radicals that are expected to H-abstract. On the other hand, as the electronegativity of $\text{EtO}\cdot$ and $\text{Me}\cdot$ increases, the H-abstraction ability is predicted to decrease, where their higher volatility must also play a major role in their fate.

As the electronegativity of $\text{PhC}(\text{Me})_2\text{O}\cdot$ relative to $\text{EtO}\cdot$ is greater, where H abstraction is observed experimentally in the former, but not latter. This can be compared to the literature,³⁷ where more electronegative *t*-BuO \cdot favors H abstraction compared to MeO \cdot . In our series, the

less electronegative radical, $\text{EtO}\cdot$, does not give recombination or abstraction, but instead only loss of $\text{Me}\cdot$. Demethylation can be accomplished by alkoxy radical structures bearing flanking methyl groups. A previous report with UM06-2X calculations also showed that methyl radical elimination is the main dissociation mechanism for peroxides after O–O bond cleavage.³⁸ The $\text{Me}\cdot$ proceeds by H abstraction to form CH_4 . We find that $\text{PhC}(\text{Me})_2\text{O}\cdot$ abstracts a hydrogen from SiOH on the particle surface. A secondary reaction between $\text{SiO}\cdot$ and $\text{PhC}(\text{Me})_2\text{O}\cdot$ to form $\text{SiOOC}(\text{Me})_2\text{Ph}$ is possible, but was not discerned. $\text{EtO}\cdot$ and $\text{Me}\cdot$ are noted, as our trapping does not address the problem of direct detection that follows the radicals themselves on and off the surface. We assumed a facile volatility and transit off of the surface, where CH_4 increase in the surrounding medium over time. Adsorption of $\text{EtO}\cdot$ is lower than $\text{PhC}(\text{Me})_2\text{O}\cdot$ or else there would have been dimerization to reach **8**, which is not observed.

Table 2. Radical ionization potential (IP), electron affinity (EA), and H-abstraction

radical	electronegativity (IP + EA)/2 (eV)	H-abstraction	comment
PhC(Me) ₂ O [•]	4.49		observed
EtO [•]	5.72	only H-loss observed	not observed
Me [•]	5.65		observed
(HO) ₃ SiO [•] ^a	5.08	more H- abstraction than EtO [•] but less than PhC(Me) ₂ O [•]	predicted greater than Et [•] and less than PhC(Me) ₂ O [•]

^a Model for surface siloxy radical.

A comparison of DFT calculated energy difference between alkoxy radicals and corresponding siloxy radical species is instructive. A comparison of calculated energy difference between H-bonding of alkoxy radical and alcohol systems is shown in Figure 4. Notice that the RO[•]···HOSi(OH)₃ hydrogen bonding is stronger by 13.7-13.9 kcal/mol compared to the ROH···OSi(OH)₃ hydrogen bonding (cf. **I** and **III** with **II** and **IV**). There are also similar stabilizing effects for H-bonding arrangements of EtO[•]···HOSi(OH)₃ (-8.4 kcal/mol) and PhC(Me)₂O[•]···HOSi(OH)₃ (-10.3 kcal/mol) compared to their separated species, respectively. Although, the PhC(Me)₂O[•] forms a slightly more stable H-bond than EtO[•] with HOSi(OH)₃. The

related H atom transfer of surface SiOH groups, are similarly expected not to proceed at any significant rate.

From a hydrogen bonding point of view, cumyloxy radical is a candidate for both $\text{SiOH}\cdots(\pi)\text{PhC}(\text{Me})_2\text{O}\bullet$ and $\text{PhC}(\text{Me})_2\text{O}\bullet\cdots\text{HOSi}$ hydrogen bonding. As has been reported, silanol groups or silanols occupied with water can bind to naphthalene by $\pi\cdots\text{HOSi}$ bonding.²⁹ Similarly, alkoxy radicals can form a weak $\text{RO}\bullet\cdots\text{HOR}$ hydrogen bond to alcohols, although the activation energy for H-atom transfer is high,³⁹⁻⁴¹ which is consistent with our DFT results.

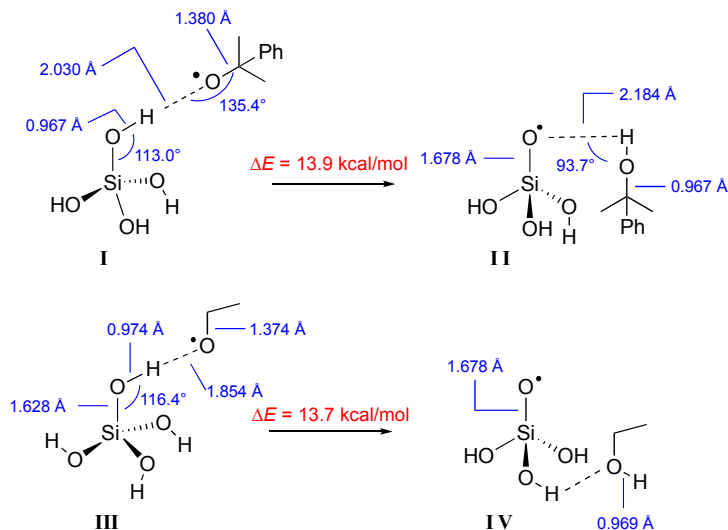


Figure 4. Calculated energy difference between H-bonded isomers.

Similar to the H-abstraction analysis in Figure 4 and Table 2, the reactions were analyzed with mathematical deductions on the particle surface. What we deduce next is a facet inhibiting radical recombination to form the symmetrical product **3**, where radicals can abstract an H atom from the SiOH group (or adsorbed water) on the particle surface. Eq 5 shows the calculated

number of silanol groups per gram using the known surface area ($200 \text{ m}^2/\text{g}$) and the known $4 \text{ SiOH}/\text{nm}^2$ of silica. Eq 6 uses Avogadro's number (N_A) in the conversion of the number of silanol groups per gram of silica found using eq 4 to moles of silanol per gram. The presence of SiOH groups attenuates cumyloxy radical migration due to H-abstraction reactivity, as we will see next.

SiOH groups per gram particle = surface area (m²/g) × (silanol groups present/m²).....(5)

$$\text{SiOH groups (moles)/g particle} = \frac{\text{number of SiOH groups/g particle}}{N_A} \dots \dots \dots (6)$$

Figure 5 shows that cumyloxy radical can bypass ~2-3 SiOH groups before H-abstraction becomes competitive. After the 2-3 SiOH groups, there is a shift toward a more equally balanced formation of the cumyloxy radical recombination and H abstraction processes. Finally, with more than 3 SiOH encounters, now there is a shift toward the H abstraction reaction being formed. The maximum number of SiOH groups that the cumyloxy radical encounters over a given distance is shown in eq 7. Eq 7 shows that the radical length is taken as 0.66 nm. These calculations would allow for the smallest SiOH value to be 1 as the estimated area of the radical would be 0.28 nm^2 , and estimating how many SiOH are in this area would be $0.28 \text{ nm}^2 \times 4 \text{ SiOH per nm}^2 = 0.76 \approx 1 \text{ SiOH}$ in the radical area. Table 1 shows the yield of cumyl alcohol **4** in the photoreaction. The H-abstraction route to cumyl alcohol **4** was competitive to radical recombination to **3** at high loadings of **2**. Surface SiOH groups to propagate silicate-type SiO₂ radicals are minimal or else diffusion distances would have been 0.5 nm given the distance

between SiOH groups on the surface. Lower loading of **2** was used in the photoreaction, where it seems possible that the SiOH position is sterically hindered by the surface of the nanoparticle itself. Polymer studies have provided information on the cumyloxy radical H-atom abstraction limited by steric hindrance imposed from methyl substituents on secondary positions within poly(propylene) and poly(isobutylene).³⁷

maximum SiOH groups bypassed by the cumyloxy radical =
 radical migration distance \times radical length \times 4 SiOH per nm².....(7)

We find a relationship between migration distance of cumyloxy radical and its tendency to dimerize or abstract a hydrogen atom from the surface. Cumyloxy radical gives recombination in a 2:1 preference to abstraction at high loading of **2** (entry 1). On the other hand, when the loading of **2** decreases (entry 5), H abstraction is observed in an elevated 3.3:1 preference over recombination. These ratios are measured by the relative yields of **3** and **4**. The acetophenone **5** product is also observed by cumyloxy radical's loss of $\text{Me}\cdot$. The products from volatile radicals $\text{Me}\cdot$ and $\text{EtO}\cdot$ were difficult to quantitate. $\text{Me}\cdot$ can abstract a H-atom and be detected as CH_4 ; $\text{EtO}\cdot$ loses an H-atom and is detected as CH_3CHO . Despite their volatility, detection in a solution-phase reaction (condition B) was more accessible than in the headspace of an air/particle reaction (condition A), as seen in Table 1.

The cumyloxy radical migration on a silica surface is rationalized because of relatively low H-bonding strength to the surface. For example, the experimental diffusional activation energy was reported to be 1.9 kcal/mol for 2,2,6,6-tetramethylpiperidine-1-oxyl radical from hydrogen bonding to the surface SiOH.⁴² In passing, we also mention a report on longitudinal-

field muon spin relaxation showing a diffusion activation energy to be 2.6 kcal/mol for $\cdot\text{CCl}_2\text{CH}_3$ radical due to association to the surface SiOH .⁴³

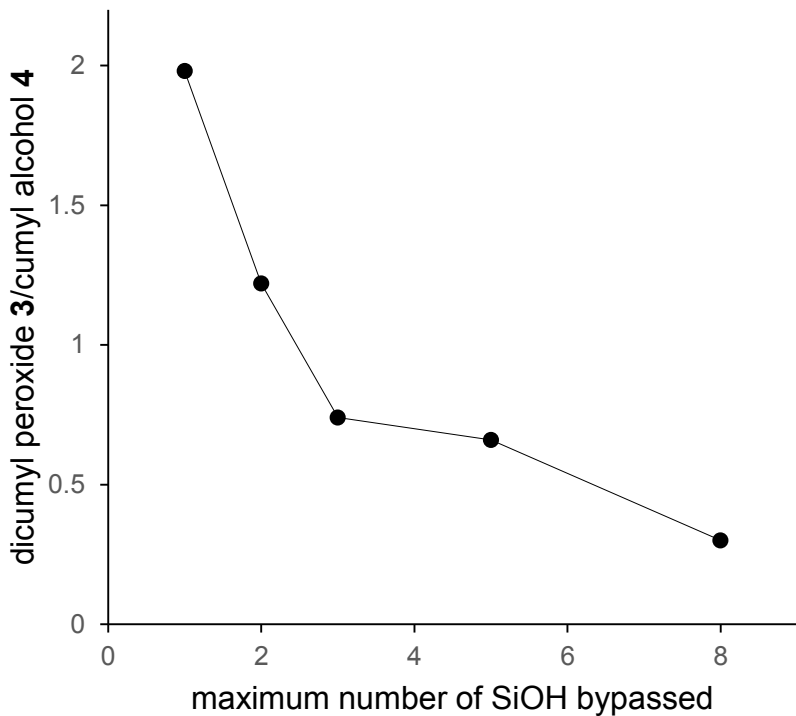


Figure 5. Maximum number of SiOH bypassed by the cumyloxy radical as it migrates linearly on the particle surface as deduced by the formation of recombination (**3**) and abstraction (**4**) products. The Y-axis represents a measure of recombination (**3** formation) vs H-abstraction (**4** formation).

Mechanism. Upon excitation, nanoparticle-adsorbed **1** transfers energy to the O–O bond of **2** resulting in its homolysis. Our previous work⁵ suggested this to be a Dexter (triplet) energy transfer process. In the present work, we found that (i) the higher percent the nanoparticle was loaded with **2**, a greater amount of **3** was formed selectively by radical recombination. (ii) Cumyloxy radical migration distance extended as far as 2.9 nm as measured by its recombination, (iii) HPLC and ¹H NMR spectroscopy enable the SPR approach, with the latter detection improved due to the symmetry of product **3** (detection limit, 0.12 mM). The percent coverage of peroxide **2** on the nanoparticle surface was 0.87-13.8%, which compares favorably to De Mayo and co-worker's radical combination to symmetrical products requiring 10-50% coverage of 1-(4-methylphenyl)-3-(4-methoxyphenyl)-2-propanone.^{44,45} Alkoxy radicals tend not to react at the peroxide O–O bond,⁴⁶ whereas carbanions can attack the peroxide O–O bond to form ethers by electrophilic alkoxy "RO⁺" transfer,⁴⁷ where ethers⁴⁸ or other downstream peroxide compounds are not observed in our case. (iv) The results from DFT calculations provide evidence that the O–O bond energy in symmetrical **3** is increased by 1.8 kcal/mol upon exchange with unsymmetrical **2**, which contributes to enriching to dimerize PhC(Me)₂O[•] to **3** on the particle surface. (v) The reaction disfavors the formation of SiO[•] surface radicals due to endothermicity of 17.0-18.2 kcal/mol based on DFT calculations. The H-atom loss of EtO[•] to reach **6** and H-atom gain of Me[•] to reach **4** may occur on the surface or in the gas phase. Yet under higher energy conditions, SiO[•] has been detected by ⁶⁰Co γ irradiation of SiOH^{49,50} and by •OH reactions.⁵¹ (vi) The cumyloxy radical recombination increased relative to cumyl alcohol formation by surface H-atom transfer when bypassing <3 SiOH groups, otherwise cumyl alcohol formation is competitive. Reduction of radical migration would be expected on a surface with greater concentration of silanol groups, e.g., on zeosil silica.⁴⁹

In summary, the SPR strategy is simple, it capitalizes on the retention of the heavier cumyloxy radical than the lighter volatile radicals to facilitate self-sorting and thus the formation of the symmetrical product **3**. The SPR method described here is appropriate for the detection of a radical migration up to 2.9 nm in the present case. There is increased migration of cumyloxy radical at lower loadings of **2** compared to higher loadings. But there are competitive paths due to higher loading of **2**, one is SiOH H-abstraction to form cumyl alcohol **4**. With a higher O–O bond energy and lower volatility, product **3** enriches itself since reagent **2** generates the more labile EtO• and Me• upon sensitized decomposition. Over extended photolysis times Me• formation increases by PhC(Me)₂O• demethylation, which attenuates the SPR assessment, as there is less of the alkoxy radical to dimerize to symmetrical product **3**.

Conclusion

The SPR method that quantifies radical surface migration will have limitations. It requires detectable recombination product quantities by HPLC and ¹H NMR spectroscopy. Despite the limitation, our findings provide a new approach important to radical migration on nanoparticles. Our conclusion is that SPR is appropriate for radical migration studies on particle surfaces, suggesting possibilities to this methodology might work on other radicals, such as free radicals on airborne fine particulate matter.

While there is value for research in control over surface radical delivery and persistence, especially when radical persistence is detected in airborne particulate matter, the question is what technology can be developed to make inroads. Current EPR methods detect surface radicals, where differentiating between radical propagation *versus* migration presents challenges.

Furthermore, mechanistic understanding of radicals at the air/solid interface lags well behind that of radical reactions in homogeneous solution.

Future mechanistic efforts are needed for analyzing the properties of radicals at interfaces. Particle designs could include (i) use of a particle system with variable tumbling rates to enhance surface radical diffusion and facilitate transiting off of volatile radicals, in particular given the importance of volatile alkoxy radicals as reactive intermediates in atmospheric chemistry.⁵²⁻⁵⁶ (ii) An alkoxy radical surface migration system can be studied experimentally based on surface silanols with increasing water content to assess effects on the radical migration distance.⁵⁷⁻⁶⁰ Simulations of alkoxy radical surface migration can also be studied by silica cluster models with quantum mechanics/molecular mechanics methods.⁶¹ (iii) A complementary SPR/EPR method can be developed for product distribution by radical recombination, and assist in distinguishing between stationary and migratory surface radicals. (iv) Radical migration on surfaces by mass spectrometry can be investigated to homolyze $\text{R}^{18}\text{O}^{18}\text{OR}$ and $\text{R}^{16}\text{O}^{16}\text{OR}$ for recombination to $\text{R}^{18}\text{O}^{16}\text{OR}$ peroxides (Figure 6), which is reminiscent of isotope-sorting recombination that has been achieved.^{62,63}

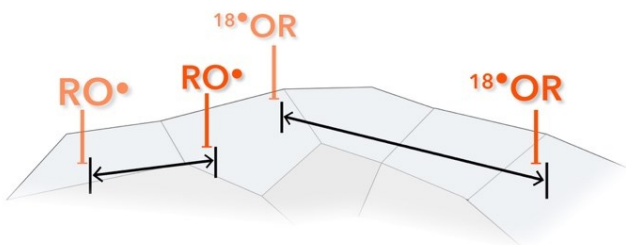


Figure 6. A schematic of our air/solid heterogeneous system with a dispersion of $\text{R}^{18}\text{O}^{18}\text{OR}$ and $\text{R}^{16}\text{O}^{16}\text{OR}$ peroxides on a nanoparticle. Upon irradiation, the resulting mixed peroxides $\text{R}^{18}\text{O}^{16}\text{OR}$ will provide indirect evidence of surface alkoxy radical migration.

Experimental

General. Acetophenone, cumene hydroperoxide, cumyl alcohol, 4,4'-dimethylbenzil **1**, and dicumyl peroxide **3** were purchased from Sigma Aldrich and used as received. Acetonitrile, acetonitrile-*d*₃, chloroform-*d*, dichloromethane, methanol, and HPLC grade water were purchased from VWR and used as received. Cumylethyl peroxide **2** was synthesized in 74% yield and 82% purity by a literature procedure.⁵ ¹H NMR data were collected on a Brucker Avance 400 MHz instrument. HPLC data were collected on an Agilent Technology instrument (column: ZORBAX Eclipse XDB-C18).

Sample Preparation. Unfunctionalized hydrophilic fumed silica nanoparticles (200-300 nm diameter, 200 ± 25 m²/g surface area) were purchased from Sigma Aldrich and washed in a Soxhlet extractor with dichloromethane and methanol prior to use. The nanoparticles were then dried in a furnace at 110 °C for 24 h. 4,4'-Dimethylbenzil **1** and cumylethyl peroxide **2** were co-adsorbed onto the nanoparticles in a manner similar to that described previously.^{5,64} The 4,4'-dimethylbenzil **1** (330 µmol) and cumylethyl peroxide **2** (amounts ranging from a high of 108 µmol to a low of 6.8 µmol) were dissolved in 5 mL dichloromethane and stirred with 1.0 g of nanoparticles for 30 min in a 25-mL Teflon bottle. The dichloromethane was then evaporated by use of a vacuum leaving the reagents adsorbed, assumed to be uniformly distributed on the nanoparticles. This equated to percent loading of adsorbed sensitizer **1** and peroxide **2** in the amounts of 25% and 0.87-13.8%, respectively. Notice that the surface was loaded with high sensitizer to low peroxide ratios, that is, sensitizer-to-peroxide loading ratios ranging from 3:1 up to 49:1. We had previously reported on sensitizer-to-peroxide loading ratios of up to 4:1,⁶⁴ and

there have been reports of high dye polymer loadings.⁶⁵ These ratios of sensitizer-to-substrate were high for the photosensitized homolysis of **2**, and is purposely dissimilar to most literature on sensitization reactions that use very low sensitizer quantities.⁶⁶ This permitted use to maintain an optimal sensitizer-peroxide distance of 7 Å for the triplet sensitized homolysis, as we had previously established.⁶⁴ Close intermolecular distances afford high yields of triplet-sensitized O–O homolysis of peroxides. Another paper has been published on such a reaction.⁶⁷

Photosensitization reactions were carried out using a 5-mL airtight vial. The nanoparticles were tumbled by a stirring paddle during the irradiation, where samples were placed at a distance of ~10 cm midpoint between two 400-W metal halide lamps delivering light (280 < λ < 700 nm). The fluence rate at a mid-point in between the bulbs was 21.8 ± 2.4 mW/cm².⁶⁸ Upon irradiation, the temperature of the particles was found to rise by ~10 °C, as we had detected in a similar system previously.⁵ This was measured by a thermos couple probe attached to an IR thermometer. After photolysis, compounds were desorbed from the nanoparticle surface by stirring with 2-mL acetonitrile for 20 min. Particles in the acetonitrile were removed passing through a syringe filter. Acetonitrile was then completely evaporated and the residue analyzed by HPLC (C-18 reverse phase column, 80% MeOH-H₂O v/v mobile phase, 1-mL/min flow rate) and ¹H NMR spectroscopy (with acetonitrile-*d*₃). Even with modest peroxide **2** surface loadings of 0.9–13.8%, and ~15% conversion of the reaction, dicumyl peroxide product **3** was readily detected by HPLC and ¹H NMR spectroscopy. To analyze the volatile products released off the silica surface after photolysis, head space analysis of 1-mL gas was drawn up in a glass syringe and slowly bubbled into chloroform-*d* and analyzed by ¹H NMR spectroscopy. For heterogeneous reactions, due to the apparatus design, filtering of light below 300 nm was not carried out as was done in previous work with homogeneous solutions.¹⁸

Without sensitizer **1**, control photoreactions showed conversion of cumylethyl peroxide **2** (108 $\mu\text{mol/g}$) with ($280 < \lambda < 700 \text{ nm}$) light to dicumyl peroxide **3** in <0.002%, whereas the sensitized reaction produced >1,000-fold more. For the homogeneous photoreactions, sensitizer **1** (0.01 mM) and peroxide **2** (0.1 mM) in acetonitrile-*d*₃ were irradiated in an NMR tube for 1 h using the 400-W metal halide lamp system.

Theoretical Section. DFT calculations were carried out to analyze structural aspects and reactions of peroxides **2-4**, and alkoxy radicals PhC(Me)₂O• and EtO•. All calculations were conducted with the Gaussian16 program (revision C.01).⁶⁹ We used UM06-2X along with Pople's 6-31G(d,p) basis set. Thermal corrections to 298 K were used in the reported energies. The quality of the energetics with the 6-31G(d,p) basis set was reasonable in comparison to UM06-2X calculations with the use of a larger basis set [6-311+G(3df,2p)].²⁴ Vibrational frequency calculations were conducted to analyze all stationary points. The TS structures were verified by both frequency calculations and by tracing their internal reaction coordinates (IRC). To compute the O–O bond cleavage, the endothermicity of peroxides **2-4** relative to their corresponding alkoxy radicals was computed by comparing optimized energies of the former to the latter as radical pairs separated by a distance of 3.0 Å. Simulations of $\pi\cdots\text{HO}$ and $\text{O}\cdots\text{HO}$ hydrogen bonding of PhC(Me)₂O•, EtO•, PhC(Me)₂OH, EtOH, or C₆H₆ were carried out with (HO)₃SiOH and (HO)₃SiO• molecules in the gas phase as an approximate model of silanol or silanoxy sites at the air/solid interface.

ORCID

Sarah J. Belh: 0000-0003-2655-6237

Goutam Ghosh: 0000-0002-2021-4589

Alexander Greer: 0000-0003-4444-9099

Acknowledgement

We acknowledge the National Science Foundation (CHE-1856765). This work used Comet, the Extreme Science and Engineering Discovery Environment (XSEDE) cluster at the San Diego Supercomputer Center, which is supported by the NSF (ACI-1548562) through allocation CHE-2000050. We thank Leda Lee for the graphic arts work.

Supporting Information

Supporting Information is available, which includes UV-vis and ^1H NMR spectra, an HPLC trace, details of sensitizer **1** and peroxide **2** loading onto nanoparticles, compound detection, results of temperature studies, illustrations of grids depicting compound loading and migration on the nanoparticle surface, and descriptions of energies and geometries of stationary points.

References

1. Sim, S.; Forbes, M. D. E. Radical–triplet Pair Interactions as Probes of Long–range Polymer Motion in Solution. *J. Phys. Chem. B* **2014**, *118*, 9997-10006.
2. Forbes, M. D. E.; Dukes, K. E.; Myers, T. L.; Maynard, H. D.; Breivogel, C. S.; Jaspan, H. B. Time-resolved Electron Paramagnetic Resonance Spectroscopy of Organic Free Radicals Anchored to Silica Surfaces. *J. Phys. Chem.* **1991**, *95*, 10547-10549.

3. Forbes, M. D. E.; Myers, T. L.; Dukes, K. E.; Maynard, H. D. Biradicals and Spin-correlated Radical Pairs Anchored to SiO₂ Surfaces: Probing Diffusion at the Solid/Solution Interface. *J. Am. Chem. Soc.* **1992**, *114*, 353-354.
4. Forbes, M. D. E.; Ruberu, S. R.; Dukes, K. E. Dynamics of Spin-polarized Radical Pairs at the Solid/Solution Interface. *J. Am. Chem. Soc.* **1994**, *116*, 7299-7307.
5. Ghosh, G.; Greer, A. A Fluorinated Phosphite Traps Alkoxy Radicals Photogenerated at the Air/solid Interface of a Nanoparticle. *J. Phys. Org. Chem.* **2020**; e4115.
6. Sindt, A. J.; DeHaven, B. A.; Goodlett, D. J.; Hartel, J. O.; Ayare, P. J.; Du, Y.; Smith, M. D.; Brugh, A. M.; Forbes, M. D. E.; Bowers, C. R., et al. Guest Inclusion Modulates Concentration and Persistence of Photogenerated Radicals in Assembled Triphenylamine Macrocycles. *J. Am. Chem. Soc.* **2020**, *142*, 502-511.
7. DeHaven, B. A.; Goodlett, D. W.; Sindt, A. J.; Noll, N.; DeVetta, M.; Smith, M. D.; Martina, C. R.; González, L.; Shimizu, L. S. Enhancing the Stability of Photogenerated Benzophenone Triplet Radical Pairs Through Supramolecular Assembly. *J. Am. Chem. Soc.* **2018**, *140*, 13064-13070.
8. DeHaven, B. A.; Tokarski, J. T.; Korous, A. A.; Mentink-Vigier, F.; Makris, T. M.; Brugh, A. M.; Forbes, M. D. E.; van Tol, J.; Bowers, C. R.; Shimizu, L. S. Endogenous Radicals of Self-Assembled Benzophenone *bis*-Urea Macrocycles: Characterization and Application as a Polarizing Agent for Solid-State DNP MAS NMR Spectroscopy. *Chem. Eur. J.* **2017**, *23*, 8315-8319.
9. Chen, Q.; Sun, H.; Wang, M.; Wang, Y.; Zhang, L.; Hand, Y. Environmentally Persistent Free Radical (EPFR) Formation by Visible-Light Illumination of Organic Matter in Atmospheric Particles. *Environ. Sci. Technol.* **2019**, *53*, 10053-10061.

10. Jia, H.; Zhao, S.; Shi, Y.; Zhu, L.; Wang, C.; Sharma, V. K. Transformation of Polycyclic Aromatic Hydrocarbons and Formation of Environmentally Persistent Free Radicals on Modified Montmorillonite: The Role of Surface Metal Ions and Polycyclic Aromatic Hydrocarbon Molecular Properties. *Environ. Sci. Technol.* **2018**, *52*, 5725-5733.

11. Runberg, H. L.; Mitchel, D. G.; Eaton, S. S.; Eaton, G. R.; Majestic, B. J. Stability of Environmental Persistent Free Radicals (EPFR) in Atmospheric Particulate Matter and Combustion Particles. *Atmos. Environ.* **2020**, *240*, 117809.

12. Vejerano, E. P.; Rao, G.; Khachatryan, L.; Cormier, S. A.; Lomnicki, S. Environmentally Persistent Free Radicals: Insights on a New Class of Pollutants. *Environ. Sci. Technol.* **2018**, *52*, 2468-2481.

13. Feld-Cook, E.; Bovenkamp-Langlois, G. L.; Lomnicki, S. M. The Effect of Particulate Matter Mineral Composition on Environmentally Persistent Free Radical (EPFR) Formation. *Environ. Sci. Technol.* **2017**, *51*, 10396-10402.

14. Vejerano, E.; Lomnicki, S.; Dellinger, B. Formation and Stabilization of Combustion-Generated Environmentally Persistent Free Radicals on an $\text{Fe(III)}_2\text{O}_3$ /Silica Surface. *Environ. Sci. Technol.* **2011**, *45*, 589-594.

15. Truong, H.; Lomnicki, S.; Dellinger, B. Potential for Misidentification of Environmentally Persistent Free Radicals as Molecular Pollutants in Particulate Matter. *Environ. Sci. Technol.* **2010**, *44*, 1933-1939.

16. Chiesa, M.; Giamello, E.; Che, M. EPR Characterization and Reactivity of Surface-Localized Inorganic Radicals and Radical Ions. *Chem. Rev.* **2010**, *110*, 1320-1347.

17. Bakos, T.; Valipa, M. S.; Maroudasa, D. First-principles Theoretical Analysis of Silyl Radical Diffusion on Silicon Surfaces. *J. Chem. Phys.* **2006**, *125*, 104702.

18. Belh, S. J.; N. Walalawela; S. Lekhtman; A. Greer Dark-binding Process Relevant to Preventing Photosensitized Oxidation: Conformation Dependent Light and Dark Mechanisms by a Dual-functioning Diketone. *ACS Omega* **2019**, *4*, 27, 22623-22631.

19. Voloshchuk, T.; Farina, N. S.; Wauchope, O. R.; Kiprowska, M.; Haberfield, P.; Greer, A. Molecular Bilateral Symmetry of Natural Products: Prediction of Selectivity of Dimeric Molecules by Density Functional Theory and Semiempirical Calculations. *J. Nat. Prod.* **2004**, *67*, 1141-1146.

20. Bai, W.-J.; Wang, X. Appreciation of Symmetry in Natural Product Synthesis. *Nat. Prod. Rep.* **2017**, *34*, 1345-1358.

21. Edericlki, B.; Johnston, L. J.; de Mayo, P.; Wong, S. K. Surface Photochemistry: Generation of Benzyl Radical Pairs on Dry Silica Gel. *Can. J. Chem.* **1984**, *64*, 403-410.

22. Fasciani, C.; Alejo, C. J. B.; Grenier, M.; Netto-Ferreira, J. C.; Scaiano, J. High-Temperature Organic Reactions at Room Temperature using Plasmon Excitation: Decomposition of Dicumyl Peroxide. *Org. Lett.* **2010**, *13*, 204-207.

23. Greer, A.; Balaban, A. T.; Liebman, J. F. In *Chemistry of Peroxides*; Greer, A.; Liebman, J. F., Eds., Wiley: Chichester, UK, 2014; Vol. 3, pp 1-20.

24. Bach, R. D.; Schlegel, H. B. Bond Dissociation Energy of Peroxides Revisited. *J. Phys. Chem. A* **2020**, *124*, 4742-4751.

25. Sert, Y.; Puttaraju, K. B.; Keskinoglu, S.; Shivashankar, K.; Ucun, F. FT-IR and Raman Vibrational Analysis, B3LYP and M06-2X Simulations of 4-Bromomethyl-6-*tert*-butyl-2H-chromen-2-one. *J. Mol. Struct.* **2015**, *1079*, 194-202.

26. Tumanov, V. E.; Denisov, E. T., Estimation of Enthalpies of Alkoxy Radical Formation and Bond Strengths in Alcohols and Ether. *Kinet. Catalysis* **2004**, *45*, 621-627.

27. Ireton, R.; Gordon, A. S.; Tardy, D. C. Thermal Decomposition of Perfluoro-di-*t*-butyl Peroxide. *Int. J. Chem. Kinet.*, **1977**, *9*, 769-775.

28. Yaremenko, I. A.; Radulov, P. S.; Medvedev, M. G.; Krivoshchapov, N. V.; Belyakova, Y. Y.; Korlyukov, A. A.; Illovaisky, A. I.; Terent'ev, A. O.; Alabugin, I. V. How to Build Rigid Oxygen-Rich Tricyclic Heterocycles from Triketones and Hydrogen Peroxide: Control of Dynamic Covalent Chemistry with Inverse α -Effect. *J. Am. Chem. Soc.* **2020**, *142*, 14588-14607.

29. Bjarneson, D. W.; Petersen, N. O. Direct Diffusion Measurements of Naphthacene on Silica as a Function of Silanol Density. *J. Am. Chem. Soc.* **1990**, *112*, 988-992.

30. Hema, B. T.; Pant, T.; Dhondiyal, C. C.; Rana, M.; Chowdhury, P.; Joshi, G. C.; Arya, P.; Tiwari, H. Computational Study of the Intermolecular Interactions and Their Effect on the UV-visible Spectra of the Ternary Liquid Mixture of Benzene, Ethanol and Propylene Glycol. *J. Mol. Model.* **2020**, *26*, 268.

31. Casu, M. B. Nanoscale Organic Radicals on Surface, Interface, and Spinterface. *Acc. Chem. Res.* **2018**, *51*, 753-760.

32. Mas-Torrent, M.; Crivillers, N.; Rovira, C.; Vecianna, J. Attaching Persistent Organic Free Radicals to Surfaces: How and Why. *Chem. Rev.* **2012**, *112*, 2506-2527.

33. Leach, A. G.; Wang, R.; Wohlhieter, G. E.; Khan, S. I.; Jung, M. E.; Houk, K. N. Theoretical Elucidation of Kinetic and Thermodynamic Control of Radical Addition Regioselectivity. *J. Am. Chem. Soc.* **2003**, *125*, 4271-4278.

34. Yang, Z.; Yu, P.; Houk, K. N. Molecular Dynamics of Dimethyldioxirane C-H Oxidation. *J. Am. Chem. Soc.* **2016**, *138*, 4237-4242.

35. Yang, F.; Deng, F.; Pan, Y.; Zhang, Y.; Tang, C.; Huang, Z. Kinetics of Hydrogen Abstraction and Addition Reactions of 3-Hexene by OH Radicals. *J. Phys. Chem. A* **2017**, *121*, 1877-1889.

36. Heberger, K.; Lopata, A. Assessment of Nucleophilicity and Electrophilicity of Radicals, and of Polar an Enthalpy Effects on Radical Addition Reactions. *J. Org. Chem.* **1998**, *63*, 8646-8653.

37. Garrett, G. E.; Mueller, E.; Pratt, D. A.; Parent, J. S. Reactivity of Polyolefins toward Cumyloxy Radical: Yields and Regioselectivity of Hydrogen Atom Transfer. *Macromolecules* **2014**, *47*, 544-551.

38. Tabriz, M. F.; Çizmeciyani, N.; Birer, Ö.; Yurtsever, E. Energy Landscapes in Photochemical Dissociation of Small Peroxides. *J. Phys. Chem. A* **2019**, *123*, 1353-1362.

39. Dibble, T. S.; Phama, T. Peroxy and Alkoxy Radicals from 2-Methyl-3-buten-2-ol. *Phys. Chem. Chem. Phys.*, **2006**, *8*, 456-463.

40. Dibble, T. S. Intramolecular Hydrogen Bonding and Double H-Atom Transfer in Peroxy and Alkoxy Radicals from Isoprene. *J. Phys. Chem. A* **2004**, *108*, 2199-2207.

41. Davis, A. C.; Francisco, J. S. Hydroxyalkoxy Radicals: Importance of Intramolecular Hydrogen Bonding on Chain Branching Reactions in the Combustion and Atmospheric Decomposition of Hydrocarbons. *J. Phys. Chem. A* **2014**, *118*, 10982-11001.

42. Golubev V. B.; Lunina E. V.; Selivanovskii, A. K. The Paramagnetic Probe Method in Adsorption and Catalysis. *Russ. Chem. Rev.* **1981**, *50*, 421-431.

43. Rhodes, C. J.; Dintinger, T. C.; Reid, I. D.; Scott, C. A. Mobility of Dichloroethyl Radicals Sorbed in Kaolin and Silica: A Potential Model of Heterogeneous Atmospheric Processes. *Magn. Reson. Chem.* **2000**, *38*, 281-287.

44. Bauer, R. K.; Borenstein, R.; de Mayo, P.; Okada, K.; Rafalska, M.; Ware, W. R.; Wu, K. C. Surface Photochemistry: Translational Motion of Organic Molecules Adsorbed on Silica Gel and Its Consequences. *J. Am. Chem. Soc.* **1982**, *104*, 4635-4644.

45. Edericlki, B.; Johnston, L. J.; de Mayo, P.; Wong, S. K. Surface Photochemistry: Generation of Benzyl Radical Pairs on Dry Silica Gel. *Can. J. Chem.* **1984**, *64*, 403-410.

46. McMillan, G.; Wijnen, M. H. J. Reactions of Alkoxy Radicals. V. Photolysis of Di-*t*-butyl Peroxide. *Can. J. Chem.* **1958**, *36*, 1227-1232.

47. Kyasa, S.; Meier, R. N.; Pardini, R. A.; Truttmann, T. K.; Kuwata, K. T.; Dussault, P. H. Synthesis of Ethers via Reaction of Carbanions and Monoperoxyacetals. *J. Org. Chem.* **2015**, *80*, 12100-12114.

48. Oyama, R.; Abe, M. Reactivity and Product Analysis of a Pair of Cumyloxy and *tert*-Butoxyl Radicals Generated in Photolysis of *tert*-Butyl Cumyl Peroxide. *J. Org. Chem.* **2020**, *85*, 8627-8638.

49. Dondi, D.; Buttafava, A.; Zeffiro, A.; Bracco, S.; Sozzani, P.; Faucitano, A. Reaction Mechanisms in Irradiated, Precipitated, and Mesoporous Silica. *J. Phys. Chem. A.* **2013**, *117*, 3304-3318.

50. Werst, D. W.; Viokur, E. I. Radiation Damage of Alkoxy and Siloxy Ligands Bonded to Silica. *J. Phys. Chem. B.* **2001**, *105*, 1587-1593.

51. Konecny, R. Reactivity of Hydroxyl Radicals on Hydroxylated Quartz Surface. 1. Cluster Model Calculations. *J. Phys. Chem. B.* **2001**, *105*, 6221-6226.

52. Hasan, G.; Salo, V.-T.; Valiev, R. R.; Kubecka, J.; Kurten, T. Comparing Reaction Routes for ${}^3(\text{RO}\cdots\text{OR}')$ Intermediates Formed in Peroxy Radical Self- and Cross-Reactions. *J. Phys. Chem. A* **2020**, *124*, 8305-8320.

53. Bianchi, F.; Kurtén, T.; Riva, M.; Mohr, C.; Rissanen, M. P.; Roldin, P.; Berndt, T.; Crounse, J. D.; Wennberg, P. O.; Mentel, et al. Highly Oxygenated Organic Molecules (HOM) from Gas-Phase Autoxidation Involving Peroxy Radicals: A Key Contributor to Atmospheric Aerosol. *Chem. Rev.* **2019**, *119*, 3472-3509.

54. Dibble, T. S.; Chai, J. Critical Review of Atmospheric Chemistry of Alkoxy Radicals. *Adv. Atmos. Sci.* **2017**, *185*-269.

55. Kurten, T.; Moeller, K. H.; Nguyen, T. B.; Schwantes, R. H.; Misztal, P. K.; Su, L.; Wennberg, P. O.; Fry, J. L.; Kjaergaard, H. G. Alkoxy Radical Bond Scissions Explain the Anomalously Low Secondary Organic Aerosol and Organonitrate Yields From α -Pinene + NO_3 . *J. Phys. Chem. Lett.* **2017**, *8*, 2826-2834.

56. Yeh, G. K.; Clafin, M. S.; Ziemann, P. J. Products and Mechanism of the Reaction of 1-Pentadecene with NO_3 Radicals and the Effect of a -ONO_2 Group on Alkoxy Radical Decomposition. *J. Phys. Chem. A* **2015**, *119*, 10684-10696.

57. Verdaguer, A.; Weis, C.; Oncins, G.; Ketteler, G.; Bluhm, H.; Salmeron, M. Growth and Structure of Water on SiO_2 Films on Si Investigated by Kelvin Probe Microscopy and *in situ* X-ray Spectroscopies. *Langmuir* **2007**, *23*, 9699-9703.

58. Gun'ko, V. M.; Turov, V.V.; Pakhlov, E. M.; Krupska, T. V.; Borysenko, M. V.; Kartel, M. T.; Charmas, B. Water Interactions with Hydrophobic versus Hydrophilic Nanosilica. *Langmuir* **2018**, *34*, 12145-12153.

59. Leung, K.; Nielsen, Ida M. B.; Criscenti, L. J. Elucidating the Bimodal Acid–Base Behavior of the Water–Silica Interface from First Principles. *J. Am. Chem. Soc.* **2009**, *131*, 18358-18365.

60. Liu, C. C.; Maciel, G. E. The Fumed Silica Surface: A Study by NMR. *J. Am. Chem. Soc.* **1996**, *118*, 5103–5119.

61. De Lima Batista, A. P.; Zahariev, F.; Slowing, I. I.; Braga, A. A. C.; Ornellas, F. R.; Gordon, M. S. Silanol-Assisted Carbinolamine Formation in an Amine-Functionalized Mesoporous Silica Surface: Theoretical Investigation by Fragmentation Methods. *J. Phys. Chem. B* **2016**, *120*, 1660-1669.

62. Buchachenko, A. L.; Dubinina, E. O. Photo-oxidation of Water by Molecular Oxygen: Isotope Exchange and Isotope Effects. *J. Phys. Chem. A* **2011**, *115*, 3196-3200.

63. Buchachenko, A. L.; Yasin, L. L.; Belyakov, V. A. Magnet and Classical Oxygen Isotope Effects in Chain Oxidation Processes: A Quantitative Study. *J. Phys. Chem.* **1995**, *99*, 4964-5969.

64. Walalawela, N.; A. Greer Heterogeneous Photocatalytic Deperoxidation with UV and Visible Light. *J. Phys. Org. Chem.* **2018**, e3807.

65. Rodríguez, H. B.; Mirenda, M.; Lagorio, M. G.; San Román, E. Photophysics at Unusually High Dye Concentrations. *Acc. Chem. Res.* **2019**, *52*, 110–118.

66. Beeler, A. B. Introduction: Photochemistry in Organic Synthesis. *Chem. Rev.* **2016**, *116*, 9629–9630.

67. Scaiano, J. C.; Wubbels, G. G. Photosensitized Dissociation of Di-*tert*-butyl Peroxide. Energy Transfer to a Repulsive Excited State. *J. Am. Chem. Soc.* **1981**, *103*, 640-645.

68. Mohapatra, P. P.; Chiemezie, C. O.; Kligman, A.; Kim, M. M.; Busch, T. M.; Zhu, T. C.; Greer, A. ^{31}P NMR Evidence for Peroxide Intermediates in Lipid Emulsion Photooxidations: Phosphine Substituent Effects in Trapping. *Photochem. Photobiol.* **2017**, *93*, 1430-1438.

69. Frisch, M. J.; Trucks, G. W.; Schlegel, H. B.; Scuseria, G. E.; Robb, M. A.; Cheeseman, J. R.; Scalmani, G.; Barone, V.; Petersson, G. A.; Nakatsuji, H., et al. D. J. *Gaussian 16*, Revision C.01; Gaussian, Inc.: Wallingford, CT, 2016.